Meridional Overturning Circulation in a Multibasin Model. Part I: Dependence on Southern Ocean Buoyancy Forcing

JONATHAN A. BAKER, ANDREW J. WATSON, AND GEOFFREY K. VALLIS

University of Exeter, Exeter, United Kingdom

(Manuscript received 30 May 2019, in final form 2 February 2020)

ABSTRACT

The variation in the strength and structure of the overturning circulation under varying Southern Ocean buoyancy forcing, corresponding to present day, a cooler (glacial) state, and a possible future warmer state is analyzed in an idealized two-basin general circulation model connected by a southern circumpolar channel. A connection between the North Atlantic Deep Water (NADW) cell in the Atlantic basin and the Pacific Deep Water (PDW) cell in the Pacific basin occurs with a direct flow of NADW into the channel's lower cell, while PDW upwelled in the Pacific basin can flow directly into the upper wind-driven cell in the channel. The intersection of these cells along with direct zonal flows between the basins completes the interbasin circulation. The present-day Atlantic meridional overturning circulation (AMOC) in the model is upwelled both by wind-driven upwelling in the Southern Ocean and by diffusion in the Pacific and Atlantic. In a cooler climate with enhanced sea ice, the NADW cell shoals, which can then no longer flow directly into the channel's lower cell, reducing the Pacific pathway of NADW. This leads to a substantial weakening of the AMOC, suggesting buoyancy forcing changes can play a substantial role in the transition of the AMOC to a glacial state. In contrast, in a warmer equilibrium climate state with reduced AABW formation, the NADW cell strengthens and deepens. NADW is increasingly directed along the Pacific pathway, while the direct upwelling in the channel's wind-driven upper cell plays a smaller role.

1. Introduction

Over the past 20 years a great deal of progress has been made in our understanding of the processes responsible for driving the meridional overturning circulation (MOC), and its corresponding structure and transport pathways through the ocean. Numerous studies have contributed to this endeavor, including Toggweiler and Samuels (1995), Gnanadesikan (1999), Vallis (2000), Marshall and Radko (2003), Ito and Marshall (2008), Wolfe and Cessi (2009, 2011), Nikurashin and Vallis (2011, 2012), Shakespeare and Hogg (2012), Jansen and Nadeau (2016), Thompson et al. (2016), and Ferrari et al. (2017). Reviews and syntheses of many of these studies are given by Vallis (2017) and Cessi (2019).

To a large degree the global-integrated MOC is composed of two separate overturning cells. In latitude–depth space with south to the left (this orientation is used throughout the paper), a clockwise upper North Atlantic Deep Water (NADW) cell, stemming from deep water formation in the North Atlantic Ocean, overlies an anticlockwise Antarctic Bottom Water (AABW) cell in the abyssal ocean that is associated with a sinking of dense surface waters in the Southern Ocean. A large volume of NADW and AABW upwells adiabatically to the surface along sloping isopycnals in the Southern Ocean.

The ocean circulation was perhaps first considered to be a global interconnected conveyor belt by Broecker and Peng (1982), Gordon (1986), and Broecker (1987), who all provided schematics of the MOC with a transfer of water between all ocean basins, with diffusive upwelling generally imagined to be the main driver. [Numerous such schematics followed, as reviewed by Richardson (2008)]. An alternative notation, that the MOC is largely driven by westerly winds in the Southern Ocean, predates these ideas—it was discussed by Eady (1957)—but the idea languished until Toggweiler and Samuels (1995) and Doos and Coward (1997) independently suggested the Southern Hemisphere westerly winds as a mechanism to upwell NADW to the surface

Denotes content that is immediately available upon publication as open access.

Corresponding author: Jonathan Baker, jb812@exeter.ac.uk

DOI: 10.1175/JPO-D-19-0135.1

and thus drive the MOC. Most subsequent theoretical studies considered the MOC in the global-integrated sense, ignoring interbasin flows. However, observations suggest that the present-day MOC largely forms one continuous overturning cell rather than two separate cells as might be inferred from the global-integrated streamfunction. This was anticipated by Gordon (1986) and Broeker (1987) and has been better quantified by Schmitz (1995), Lumpkin and Speer (2007), and Talley (2013). In these later descriptions, much of the NADW which upwells adiabatically in the Southern Ocean is believed to flow south at the surface to form AABW and Circumpolar Deep Water (CDW) before flowing into the Pacific and Indian Oceans. The Pacific and Indian Deep Water (PDW and IDW) that form as a result of the diffusive upwelling of AABW in these basins, complete the interbasin circulation by flowing into the Atlantic Ocean via the Southern Ocean or Indian Ocean.

These pathways may have been different in the past. Proxy data suggest the AMOC became weaker during the Last Glacial Maximum (LGM), with NADW becoming shallower, perhaps no deeper that about 2 km (Lynch-Stieglitz et al. 1999; McManus et al. 2004; Curry and Oppo 2005). The glacial shoaled NADW cell is sometimes referred to as Glacial North Atlantic Intermediate Water (GNAIW) (Duplessy et al. 1988) since it is no longer "deep." Consistent with this picture, the AABW cell during the LGM expanded greatly, as suggested by a large vertical $\delta^{13}C$ gradient in the Atlantic Ocean during the LGM, with low $\delta^{13}C$ in the older, higher CO_2 concentrated waters below about 2 km (Curry and Oppo 2005). The AABW was also saltier than the Atlantic's upper cell (GNAIW) during the LGM, according to sediment proxies, in contrast with the present-day salinity distribution (Adkins et al. 2002). The change in circulation has been linked to the decrease in atmospheric CO_2 observed from ice core records in glacial time (Lauderdale et al. 2013; Watson et al. 2015) and the ageing of middepth (Burke et al. 2015) and deep water masses (Nadeau et al. 2019).

Two of the main mechanisms proposed to cause the glacial shoaling and weakening of the NADW cell during glacial periods are (i) reduced surface buoyancy fluxes (Watson and Garabato 2006; Ferrari et al. 2014; Jansen and Nadeau 2016), or (ii) a weakening or northward shift in the Southern Hemisphere westerly winds (Toggweiler and Samuels 1993, 1995; Toggweiler et al. 2006). In this paper we further investigate the first mechanism; more specifically, we perturb the Southern Ocean buoyancy forcing in a two-basin model. Overturning schematics of the present-day, glacial, and a warmer state MOC are used to depict how the MOC pathways change with variations in Southern Ocean buoyancy loss. A follow-up paper (J. A. Baker et al. 2020, unpublished manuscript, hereafter Part II) will investigate the sensitivity of the MOC to changes in Southern Ocean wind and vertical diffusivity under varying buoyancy forcings.

We choose only to vary the Southern Ocean boundary conditions in part for simplicity and in part because such changes are believed important in the transition to glacial climates (e.g., Shin et al. 2003; Liu et al. 2005; Ferrari et al. 2014; Sun et al. 2016; Jansen and Nadeau 2016; Jansen 2017). The mechanism can be expected to be significant given the importance of Southern Ocean sea ice in the water mass transformations of the present-day ocean (Abernathey et al. 2016). The NADW cell does however also depend on the buoyancy in the north (which is dependent on the surface buoyancy forcings, among other things), with the buoyancy overlap between the northern-sourced water and the southern channel shown to be key in determining the strength and depth of the largely adiabatic NADW cell (Vallis 2000; Wolfe and Cessi 2011). The depth of the NADW cell is obtained in the theory of Nikurashin and Vallis (2012) by matching the surface buoyancy in the north of the basin to the corresponding buoyancy at the channel–basin boundary. Indeed, changes in the northern boundary conditions (wind and buoyancy forcings) have also been proposed as a mechanism to alter the MOC, with the effect of ice sheets during the LGM leading to enhanced surface buoyancy and a strengthening of the NADW cell under glacial forcings (Muglia and Schmittner 2015; Klockmann et al. 2018). Changes in the northern boundary conditions are not considered in this study.

The exact mechanisms whereby changes in Southern Ocean boundary conditions affect the MOC are not wholly clear. At a basic level, Shakespeare and Hogg (2012) find an enhanced abyssal cell as the Southern Ocean buoyancy flux becomes more negative. Relatedly, Jansen and Nadeau (2016) and Jansen (2017) argue that enhanced brine rejection due to sea ice formation effectively acts as a negative buoyancy flux and indeed find an enhanced lower cell as sea ice expands in the Southern Ocean. They argue that the enhanced stratification under these buoyancy fluxes shoals the NADW cell, although only a single-basin model is used. In some contrast, Ferrari et al. (2014) hypothesize the equatorward expansion of Southern Ocean sea ice during glacial times as a mechanism to shoal and isolate the NADW cell, using a geometric argument, although no model simulations were performed. They argue the latitudinal sea ice edge separates the upper and lower cells of the MOC at the surface of the Southern Ocean due to a change in the buoyancy flux. As sea ice expands, PDW upwelled in the Pacific basin which is confined to the enhanced diffusivity

deep ocean can no longer upwell north of the sea ice and thus is isolated from the upper branch of the MOC. The NADW cell responds by shoaling above the isopycnal which outcrops at the sea ice edge. Nadeau et al. (2019) use a multibasin model to propose both mechanisms can work together by varying the Southern Ocean buoyancy fluxes, both in magnitude and in latitude, to represent enhanced buoyancy fluxes and extended sea ice. The study confirms the Jansen and Nadeau (2016) enhanced stratification mechanism in a two-basin model, extending the theory of the original study, and also validates the Ferrari et al. (2014) hypothesis. They also suggest the change in overlap between the globally averaged cell interface and the Atlantic cell interface in the north of the channel can be used to infer the connection between these cells. It is clear from these studies that changes in Southern Ocean sea ice can have a large impact on the MOC and potentially lead to shoaling of NADW in cold climates, as observed.

In this paper our main focus is on the change in the pathways taken by the MOC in response to Southern Ocean buoyancy flux changes, rather than on the exact process and mechanism that act to shoal the NADW cell. We use a model with two basins because of the potential importance of interbasin exchanges and diffusive upwelling in the Indo-Pacific Oceans (Thompson et al. 2016; Ferrari et al. 2017; Nadeau et al. 2019), and because of the evident interhemispheric nature of the overturning circulation, which as noted may have been different in glacial climates. In the present-day climate, diffusive upwelling in the Pacific basin is believed to drive the AMOC (Ferrari et al. 2017) in addition to the Southern Ocean winds (Toggweiler and Samuels 1993), but the relative importance of these processes and the pathways taken by the MOC remain uncertain. We aim to quantify the pathways taken by the MOC under varying buoyancy forcing to determine its structure in the present-day, and also how it changes in glacial and warmer than present-day climates. In section 2 we describe the model that we use (an ocean model coupled to sea ice), and in section 3 we describe the control simulation and the methodology we use to analyze the results. In section 4 we describe the results of the experiments in which we vary the buoyancy forcing and the uncertainties, and in section 5 we summarize and conclude.

2. Model setup and experiments

The Massachusetts Institute of Technology General Circulation Model (MITgcm) (Marshall et al. 1997a,b) is used with a 2.8° horizontal resolution and 20 vertical levels in a 4000-m-deep ocean, with decreasing resolution with depth, from a 50-m vertical grid space in the surface layer. An idealized domain (Fig. 1a) is used with two basins connected by a circumpolar channel in the south. The basins have an area representative of the Atlantic and Pacific Oceans, and for brevity we refer to them as "Atlantic" and "Pacific." The domain extends from 70°S to 73°N in the Atlantic basin and 65°N in the Pacific basin. The model has a longitudinal extent of 188°, with an Atlantic basin of 63.5° and a Pacific basin of 123.5°. There are two meridional land strips extending from the north of the model that represent and are referred to herein as the South America and South Africa land strips, extending to a latitude of 53° and 36°S, respectively. The Southern Ocean south of the South Africa land strip is herein referred to as the "channel." The full nonlinear equation of state for seawater is used to calculate density.

Sea ice is simulated using a fully coupled dynamic–thermodynamic model which accounts for the effects of sea ice on the buoyancy fluxes. It is based on the nonlinear dynamic–thermodynamic sea ice model with viscous-plastic rheology first employed by Hibler (1979) and modified for efficiency by Zhang and Hibler (1997), and more recently by Losch et al. (2010) for use in coupled ice–ocean models. The zero-layer thermodynamics of Hibler (1980) is used for the sea ice thermodynamics which assumes a zero heat capacity layer.

The vertical ocean diffusivity is set using the Bryan and Lewis (1979) diffusion scheme (BL79) with a surface diffusivity of approximately $10^{-5}\,m^2\,s^{-1}$ increasing to approximately $2 \times 10^{-4}\,m^2\,s^{-1}$ at depth and it is horizontally uniform (Fig. 1b). There is a large increase in vertical diffusivity at about 2 km to represent the topographical enhancement of mixing at depth caused by the generation of turbulence by internal wave breaking (Wunsch and Ferrari 2004). Convection is parameterized by adding a convective diffusivity of $100\,m^2\,s^{-1}$ to the vertical diffusivity coefficient if the ocean is statically unstable due to a decrease in density with depth.

The Gent–McWilliams (GM) eddy parameterization (Gent and McWilliams 1990; Gent et al. 1995) and the Redi scheme (Redi 1982) are used to determine the advective and isopycnal mixing effects of eddies, respectively, with the GM thickness diffusivity and Redi isopycnal diffusivity both set to $1000\,m^2\,s^{-1}$.

The model is forced at the surface by a wind stress (Fig. 1c) and heat and freshwater fluxes (Figs. 6 and 7). The inputs used in all of the model buoyancy flux experiments to calculate these forcings are zonal averages (over the real-world Atlantic and Pacific basins) of the climatological monthly averaged National Centers for Environmental Prediction–National Center for Atmospheric Research (NCEP–NCAR) reanalysis

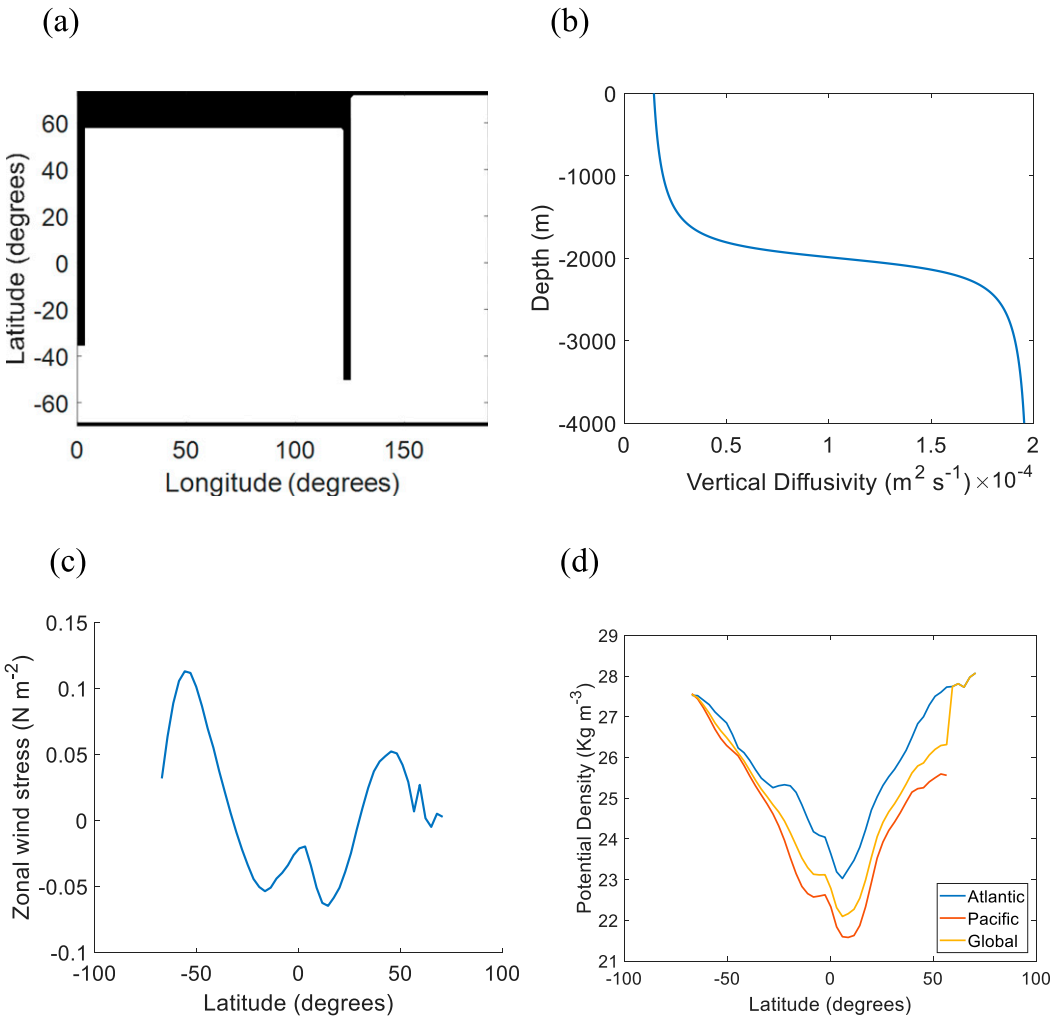

FIG. 1. (a) Bathymetry of the multibasin model. The ocean, shaded in white, has a depth of 4000 m, while land is shaded black. The basins on the left and right represent the Pacific and Atlantic Oceans, respectively. The meridional land strips in the west and center of the domain represent the South Africa and South America land strips, respectively. (b) Vertical profile of the vertical ocean diffusivity ($m^2\,s^{-1}$) used in all experiments increasing from $0.1 \times 10^{-4}\,m^2\,s^{-1}$ at the surface to $2 \times 10^{-4}\,m^2\,s^{-1}$ at the ocean floor. (c) Zonal average zonal wind stress ($N\,m^{-2}$). (d) Potential density ($kg\,m^{-3}$) of surface waters in the control experiment, zonally averaged over the Atlantic sector (blue), Pacific sector (red), and over the whole domain, referred to as global (orange).

data over the period 1981–2010 (Kalnay et al. 1996) and the surface temperature and salinity are also relaxed to observed distributions, θ^* and S^*, respectively (Levitus and Boyer 1994a,b). The NCEP forcings used are the downward shortwave and longwave radiation at the surface, the precipitation and evaporation rate, atmospheric temperature and specific humidity at 2 m, and the wind speed and zonal and meridional wind speed components at 10 m. The surface wind stress and the various components of the heat flux (i.e., the radiative, sensible, and latent heat fluxes) are calculated from these NCEP forcings using bulk formulas. The freshwater flux is calculated by combining the NCEP precipitation and evaporation rate. The surface heat and freshwater fluxes calculated from the NCEP forcings and modified by the sea ice model [referred to herein as the NCEP heat and freshwater fluxes, $Q(T_s)$ and $E - P$, respectively], and the relaxation fluxes are combined to form the boundary conditions. The heat and freshwater forcing, F_θ and F_S, are thus

$$F_\theta = \frac{Q(T_s)}{C_p \rho_0 \Delta z_s} - \lambda_\theta (\theta - \theta^*), \tag{1}$$

$$F_S = \frac{S_0}{\Delta z_s}(E - P) - \lambda_S (S - S^*), \tag{2}$$

where λ_θ and λ_S are the reciprocals of the relaxation time scales for sea surface temperature and salinity, respectively (i.e., $\lambda = 1/\tau$ where τ is the relaxation time scale), c_p is the specific heat capacity of seawater, ρ_0 is the reference density of the ocean, Δz_s is the surface layer depth, and S_0 is the reference salinity.

In regions of sea ice, the relaxation fluxes in (1) and (2) are not imposed with only the sea ice model bulk formulae used to determine the heat and freshwater fluxes. The temperature and salinity relaxation time scales are set to 3 months and 2 years, respectively, enabling both the relaxation fluxes and the NCEP heat and freshwater fluxes to play a role without unrealistic drifting of these variables (e.g., Griffies et al. 2009). The long salinity relaxation time scale leads to the freshwater flux primarily setting the salinity distribution enabling changes in sea ice brine fluxes to have a realistic effect on the surface buoyancy.

The data used to determine the NCEP heat and freshwater fluxes, and the relaxation fluxes are zonal averages of the NCEP reanalysis and Levitus and Boyer (1994a,b) datasets, respectively, but with the zonal averages applied separately over the Atlantic and Pacific sectors of the dataset. This results in zonal contrasts in the temperature and salinity forcings between the Atlantic and Pacific sectors of the model as in the real ocean (see Fig. 1d). Thus, the sea ice expands farther north in the cooler Atlantic sector of the Southern Ocean than in the Pacific sector (see Fig. 5).

We effect changes in the Southern Ocean buoyancy flux by changing the sea ice freezing point according as to whether we seek to simulate present-day conditions, a glacial state or a future warm state. Specifically, a constant sea ice freezing point is set in each of the eight experiments, with values ranging from −1.96° to 1°C (with 0.5°C increments between experiments above −1.5°C) to represent increases in Southern Ocean sea ice formation and thus changes in the surface buoyancy flux mediated through the sea ice formation rate. In the descriptions below we refer to experiments with freezing points of −1.96°, 0°, and 1°C as "warm," "present day," and "glacial" climates, respectively, noting that the experiments with a high freezing point produce more sea ice, resembling a glacial climate. The 0°C experiment produces a MOC that is most comparable with the present-day circulation (Lumpkin and Speer 2007) when compared with each of the other seven sea ice freezing point experiments (i.e., each experiment in Fig. 7). Although this is not the true sea ice freezing point, the model has an idealized bathymetry and forcings, and thus some variation from this value to obtain a present-day like MOC is not unexpected.

The NCEP data inputs and relaxation fields remain unchanged in all experiments. Therefore, surface temperature and heat flux changes are a result *only* of changes in ocean circulation and sea ice cover, so enabling the effect of changes in sea ice formation on the MOC to be isolated. Small perturbations to the sea ice formation rate can be made by slowly changing the sea ice freezing point. Thus, the gradual transition of the MOC in response to sea ice formation can be obtained. If the surface temperature was perturbed to obtain a similar transition in the MOC, the effect of sea ice changes on the circulation would no longer be isolated since there would also be changes in surface buoyancy due to the surface temperature perturbations (including nonlinear effects from the nonlinearity of the equation of state). The Southern Ocean buoyancy flux perturbation experiments are performed in section 4.

The model is spun up over several thousand years before a steady state is reached for the control state. Perturbation experiments are integrated for a further 10 000 years to ensure a steady state is reached.

3. General methodology and basic simulation

In this section we first describe the overturning circulation obtained from the control experiment. Then, in section 3b, we describe how a connection between the upper and lower cells of the MOC is enabled. We do this first in a somewhat qualitative way and then, in section 3b(2) describe a method to quantitatively separate the direct wind and Pacific pathways of NADW and the various other components of the MOC.

a. Control experiment and MOC upwelling

The control experiment uses the forcings described in section 2, with a sea ice freezing point of 0°C to represent the present day (see section 2). The control experiment net overturning circulation streamfunction calculated in depth coordinates is shown for each basin and globally integrated in Fig. 2. The net circulation is herein defined as the sum of the time-averaged Eulerian-mean and the "eddy-induced" (produced by the GM parameterization) circulations, and it is this flow that is responsible for the net advective transport of tracers.

In the Atlantic basin there is a clockwise upper NADW cell of about 13 Sverdrups (Sv; $1\,\text{Sv} \equiv 10^6\,\text{m}^3\,\text{s}^{-1}$) with deep water formation at the northern boundary, and an anticlockwise lower AABW cell at depth. In the Pacific basin, the MOC is dominated over the full ocean depth by the AABW cell, which upwells diffusively to form PDW. The global-integrated circulation is similar to the Atlantic basin overturning, but with a stronger and slightly expanded lower AABW cell. The expansion is due to the PDW cell in the Pacific basin upwelling to shallower depths than the lower cell in the Atlantic basin.

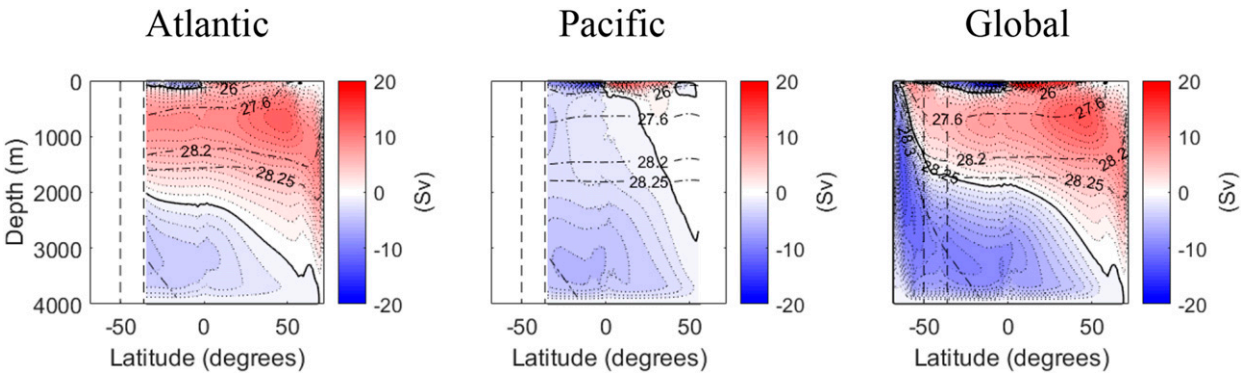

FIG. 2. Zonal-average net overturning streamfunction (Sv) in the control experiment. A sea ice freezing point of 0°C is imposed generating a MOC with a structure closest to the present day. Shown are the (left) Atlantic, (center) Pacific, and (right) global-integrated circulations. The red (positive) and blue (negative) streamfunctions are clockwise and anticlockwise circulations, respectively. The streamline contour intervals are 1 Sv. The thick solid black contour bordering the blue-shaded, anticlockwise cell is the 0-Sv streamline, separating the clockwise and anticlockwise cells. Potential density contours are represented by thin dash–dot black lines. The vertical dashed lines in the south of the domain are from left to right, the southernmost latitudes of the South America and South Africa landstrips, respectively.

This difference in the MOC structure over the whole domain compared to in the individual basins shows the importance of analyzing each basin separately to determine the ocean pathways. The global-integrated circulation in the channel is primarily controlled by the Southern Ocean westerly winds. They drive a clockwise Eulerian-mean Deacon cell and indirectly an anticlockwise eddy-induced cell.

The AMOC, specifically the circulation associated with NADW, is associated with convection in the North Atlantic basin where deep water formation occurs. For a given North Atlantic surface density distribution, the two-basin model experiments performed here suggest the volume of NADW which can be upwelled to near the surface depends on both the Southern Ocean winds and the vertical diapycnal diffusion (referred to as ''diffusion'' herein), as discussed later. Although the NADW cell in the control experiment is likely weaker than the real world present-day overturning, this is not surprising given there is no Indian Ocean diffusive upwelling and the model circumpolar channel is about half the longitudinal width of the global ocean. The remainder of this section introduces the method used to determine the MOC pathway magnitudes for a given circulation.

b. *Connections between the upper and lower cells of the MOC*

1) QUALITATIVE CONSIDERATIONS

As in previous studies, we use the idea that the upper cell in the Atlantic and the lower cell in the Pacific intersect with the lower and upper cells, respectively, in the channel (i.e., all latitudes south of the South Africa meridional land strip), under some forcings (as shall be discussed). However, we use the global-integrated streamfunction in the channel (described below) to quantitatively separate the MOC pathways at the channel–basin boundary which to our knowledge has not been considered previously. The key transfer between the upper and lower cells appears to occur just south of the channel–basin boundary.

We can see this connection between upper and lower cells from an inspection of Fig. 3, which shows the MOC in the Atlantic and Pacific basins with the global-integrated streamfunction plotted in the channel, for the experiment with a sea ice freezing point of −1.96°C. This freezing point is chosen to highlight the intersection of the overturning cells, since it leads to a deep NADW cell (with almost no AABW cell in the Atlantic basin), and thus the overlap between the upper and lower cells at the channel–basin boundary is particularly clear.

In the channel, the zonal circumpolar current flows rapidly over the whole depth of the water column, with a speed that greatly exceeds that of the meridional overturning flows, so that the density structure is more-or-less uniform over all longitudes (except near the surface where the zonal asymmetry in buoyancy forcings leads to a zonal asymmetry in surface buoyancy). The time taken for a water parcel to travel zonally around the model's southern channel is on average 14 years, and thus it would circulate around the channel about 90 times on average before the southward flowing NADW reaches the south of the domain (based on the models meridional and zonal net velocities in the channel). The overturning circulation is driven by the wind-induced Eulerian-mean and eddy-induced circulations in the channel and these are similar in structure and strength per unit longitude in each sector. The global-integrated

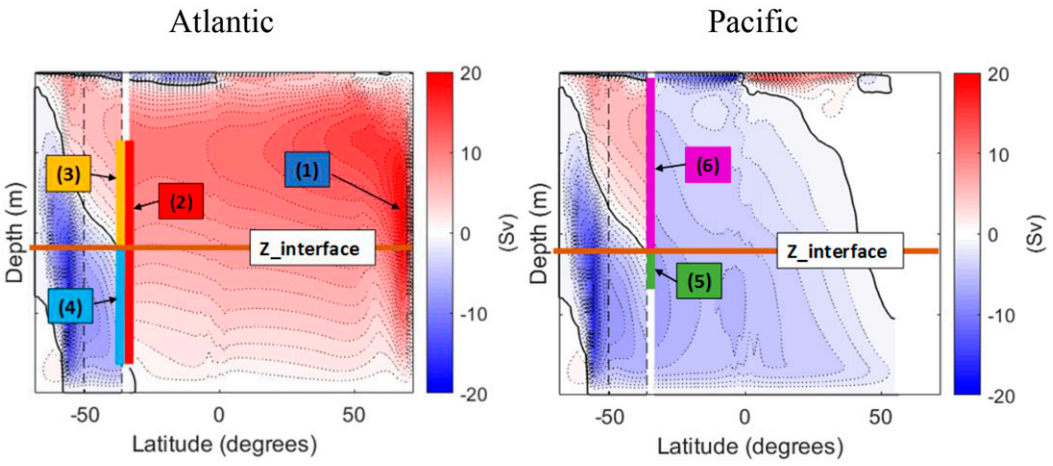

FIG. 3. Zonal-average net overturning streamfunction in the (left) Atlantic and (right) Pacific sectors when using the control forcings but with a sea ice freezing point of −1.96°C. The global-integrated streamfunction is used in the channel. Colors and contours are as in Fig. 2. The components of the overturning circulation (described in section 3b(2)) are labeled and represented by a vertical colored line at the channel–basin boundary. Each component is equal to the net flow into the channel from the applicable basin to the north over the depth of the vertical line. The components labeled are 1) NADW cell strength, 2) NADW_channel, 3) NADW_wind, 4) NADW_pac_lower, 5) PDW_sep, and 6) PDW_at. The depth of the interface between the upper and lower cells (i.e., the depth of the 0-Sv contour) of the global-integrated circulation at the channel–basin boundary, labeled z_interface is represented by the horizontal line at middepth. Component 3 is modified slightly when there is a net zonal flow of NADW into the Pacific basin above z_interface.

channel net overturning circulation is thus, to a first approximation, representative of the flow in both the Atlantic and Pacific sectors (when the continuity flows described below are neglected).

The barotropic (depth-integrated) streamfunction is shown in Fig. 5d. The strong zonal transport in the channel is clear along with a meander in the streamlines, particularly around the South America landstrip, as seen in the real world. This is caused primarily by the geometry of the model with a longer South America than South Africa landstrip combined with the strong zonal flows, which lead to a net northward and southward flow in the Atlantic and Pacific sectors, respectively. These continuity flows cancel out when zonally integrated, and taking a zonal average is appropriate due to the dominant zonal flows. We calculate the zonally integrated streamfunction at a given latitude for reasons of computational convenience. An alternative would be to integrate along the barotropic streamlines, but we show in section 4d that the error in the components calculated using the latitude integrated streamfunction is small and compare them with the components calculated in density coordinates in which the standing eddies are accounted for. The global-integrated flow is only truly a good assumption south of 42°S where the zonal flow dominates (i.e., north of the meander in the barotropic streamlines but south of the channel–basin boundary at 36°S where we calculate the components). The uncertainty in the components due to this is also shown to be small in section 4d.

The global-integrated net circulation's cell interface (i.e., the interface between the upper and lower cells) at the channel–basin boundary (labeled as "z_interface" in Fig. 3) may then be used in a calculation of the MOC components: flows coming from the northern basins which enter the channel join the upper cell if they enter above this depth, and the lower cell if they are below it.

2) QUANTITATIVE DETERMINATION OF MOC PATHWAYS AND OVERTURNING COMPONENTS

The NADW cell in the Atlantic basin and the PDW cell in the Pacific basin of a multibasin model can flow into the global-integrated lower and upper cells of the channel, respectively, at the channel–basin boundary (i.e., the upper and lower cells intersect). Thus, NADW in the upper cell, flowing into the channel from the Atlantic basin (referred to in this paper as "NADW_channel" and labeled as number 2 in Fig. 3) remains in the upper cell of the channel if it is above the interface depth, or flows directly into the lower cell of the channel if it is dense enough to be below that depth: we refer to these components as "NADW_wind" and "NADW_pac_lower," respectively, where the suffixes refer to the return pathways they take (see below). They are labeled as numbers 3 and 4 in Fig. 3.

The NADW flowing into the channel must upwell to a shallower depth before it can flow north in the Atlantic basin as less dense intermediate waters. The two components described above follow different pathways, either 1) the direct wind pathway in the channel's upper cell (NADW_wind), or 2) the Pacific pathway with diffusive upwelling in the Pacific basin (NADW_pac). The latter pathway of NADW first upwells in the channel before being converted to AABW, or it flows directly from the Atlantic to the Pacific basin via zonal flows with no upwelling.

The NADW_wind component is NADW flowing into the channel's upper wind-driven cell above the channel cell interface at the channel–basin boundary. It is consequently upwelled adiabatically in the Southern Ocean, where it is lightened at the surface by positive buoyancy fluxes and flows northward back into the Atlantic basin.

The remaining component, NADW_pac_lower, entering below the channel's cell interface, also upwells adiabatically in the Southern Ocean, before downwelling farther south. The water upwells toward the surface where it densifies by negative buoyancy fluxes, flows southward, and sinks to form AABW. This is believed to occur in the present-day ocean (Cessi 2019). The AABW formed in the far south of the model domain flows north into the Pacific basin at depth (in the present-day ocean some also flows into the Atlantic basin, but in the circulation of Fig. 3 this is negligible). The AABW upwells diffusively in the Pacific basin to form PDW before returning to the channel at shallower depths.

There is also a direct zonal pathway for NADW to enter the Pacific basin via the circumpolar channel, as discussed by Ferrari et al. (2017). Any direct zonal flow of NADW below the z_interface is already accounted for in the NADW_pac_lower component. However, if there is a zonal flow of NADW into the Pacific basin above the z_interface, a proportion of the NADW_wind component defined above is instead upwelled in the Pacific basin. Therefore, a slight modification is made to NADW_wind to account for this zonal flow (if present). The zonal flow is equal to the northward flow into the Pacific basin above the z_interface and is referred to as NADW_pac_upper. If there are two maxima in the south of the Pacific basin, any NADW which flows north above the lower maximum is included in NADW_pac_upper. Thus, NADW_pac_upper and NADW_pac_lower separate the upper and lower pathways of NADW origin waters flowing into the Pacific basin. Combining these components gives the total Pacific pathway, referred to herein as NADW_pac.

The sum of the direct wind and Pacific pathway of NADW (NADW_wind and NADW_pac, respectively) is equal to the flow of NADW into the channel (NADW_channel).

There is a third component to the NADW in our model, which does not however enter the channel. A significant volume of NADW formed in the North Atlantic in Fig. 3 upwells within the Atlantic basin due to the clockwise eddy-induced circulation in the north where isopycnals outcrop and also due to diffusive upwelling in this basin (although as is shown in section 4d, this component is smaller when calculating the components using the more appropriate isopycnal coordinates as opposed to depth coordinates which are described in the following sections).

The PDW flowing into the channel from the Pacific basin can flow along three possible routes with all three likely to be important in the present-day ocean. PDW can flow into the channel below the channel–basin cell interface and thus flow into the channel's lower cell. This water is completely isolated from the Atlantic basin's NADW cell and thus does not contribute to the NADW cell strength (the Atlantic basin lower AABW cell is also completely isolated in this way). It is herein referred to as ''PDW_sep'' (component 5 in Fig. 3). The remainder of the PDW, entering above the channel cell interface, is either upwelled further in the channel by the upper wind-induced circulation before flowing northward into the Atlantic basin, or it flows directly into the Atlantic basin without further upwelling via the direct zonal pathway. These latter pathways of PDW into the Atlantic basin are referred to here as ''PDW_at'' (component 6 in Fig. 3). This component is not displayed in later figures since by continuity, it should equal the ''NADW_pac'' component (see section 4d).

The pathways calculated in this study are only the zonal-average annual-average advective pathways and thus water flowing into the lower and upper cells may in fact flow northward and southward, respectively, at the surface due to zonal variations in the density and buoyancy fluxes in the channel. These differences are likely to largely cancel out due to the barotropic streamline meandering gradually (except around South America), particularly at the southern latitudes of the channel where the interface between the channel's upper and lower cells outcrops at the surface. While this is a caveat of our method when using depth coordinates, the isopycnal coordinate net pathways calculated in section 4d are exact.

Using the approach outlined above to separate the direct wind and Pacific pathways of the AMOC, the variation in the MOC with varying Southern Ocean buoyancy forcing will now be described.

4. Analysis of buoyancy flux experiments

In this section we describe various experiments that transition the circulation from a potential future ''warm''

low-ice state, to a ''present-day'' state, and finally a ''glacial'' state. In all cases we change the buoyancy fluxes in the Southern Ocean. As mentioned earlier, these fluxes are varied by altering the sea ice freezing point to bring about changes in sea ice formation and brine rejection. All other forcings remain unchanged. The expansion of sea ice with an increased freezing point leads to brine rejection in regions of sea ice formation, and freshwater release farther north where the sea ice melts. Thus, the buoyancy fluxes in the far south become more negative while just to the north they become more positive. The experiments performed enable the effects of changes in sea ice formation to be analyzed with any temperature changes being only a result of the effect of sea ice on the circulation. The atmospheric temperature and incoming radiative fluxes are not changed (although sea ice reduces the atmosphere–ocean heat transfer).

Figure 4 shows the overturning circulation simulated in the model with sea ice freezing points of −1.96°, 0°, and 1°C. The distribution of sea ice in the Southern Ocean and the zonal-average buoyancy fluxes in these experiments are shown in Figs. 5 and 6, respectively. The variation of the MOC components under varying Southern Ocean sea ice freezing rates (and also varying Southern Ocean buoyancy fluxes) are shown in Fig. 8, while Fig. 9 displays the variation of the Atlantic NADW cell and global-integrated cell interfaces at the channel–basin boundary. Figure 10 shows schematics of the major pathways in the three simulations shown in Fig. 4.

a. Future circulation

Using a sea ice freezing point of −1.96°C generates a circulation which has no AABW cell in the Atlantic basin in contrast to the present-day control circulation (see section 3a). This simulation could be indicative of the circulation in a equilibrated warmer climate in which there is much reduced sea ice and AABW formation in the Southern Ocean.

Figure 4a shows the overturning streamfunction in this −1.96°C freezing point experiment (the same as Fig. 3) and Fig. 10a depicts the primary overturning circulation pathways.

The annual-average buoyancy flux is slightly positive in the far south of the domain (Fig. 6a), with only seasonal AABW formation which has a lower density than in the present-day resulting in a weakly stratified abyssal ocean. Figure 7a shows the variation of the surface buoyancy flux at the surface over the whole domain, while Fig. 7b shows the zonal variation of the buoyancy flux in the far south of the domain. The buoyancy flux is positive at all longitudes in the far south, except at the longitude of South America where it is negative. However, the large decrease at this longitude is due to the zonal contrast in surface buoyancy between the cooler Atlantic and warmer Pacific sectors, coupled with the strong eastward flow which leads to a negative buoyancy flux. Thus, we suggest it is due to the large zonal temperature advection as opposed to being associated with AABW formation. The lower anticlockwise eddy-induced cell in the channel therefore does not upwell to the surface in the far south of the domain (in contrast to the control), since a negative buoyancy flux is required for a poleward surface flow. The water mass flowing into the Pacific basin therefore has approximately the same density as the NADW flowing into the channel's lower cell (see Fig. 10a) with almost no densification of the upwelled NADW required. There is a negative buoyancy flux in the south of the domain in the Southern Hemisphere winter months due to a negative zonal-average heat flux which likely explains the slight densification of NADW after it upwells in the channel's lower cell. Since the zonal-average freshwater flux remains very small in this region, the densest AABW is only slightly denser than that of NADW (see Fig. 4a).

The NADW cell strengthens to ~19.5 Sv, flowing into the channel almost all the way to the ocean floor due to the absence of an AABW cell. Therefore, there is a significant difference between the depths of the Atlantic NADW cell (~3650 m) and the global-integrated cell interface, z_interface (~2250 m) at the channel–basin boundary (see Fig. 9), and thus a large ~1400-m overlap between the NADW cell and the channel's lower cell.

Most of the ~11 Sv of NADW flowing into the channel (NADW_channel) is below the z_interface and thus the primary pathway, which accounts for ~7 Sv of NADW_channel, is along the lower route of the Pacific pathway (NADW_pac_lower, which is equal to NADW_pac in this case). Only a small volume (~4.1 Sv) of NADW flows along the direct wind pathway (NADW_wind; see Fig. 8 and Fig. 10a). The main cause of the increase in the strength of the AMOC (i.e., the NADW cell in the Atlantic basin) relative to the more present-day like control circulation (described in section 3a) is the ~5-Sv increase in upwelling of NADW in the Atlantic basin to ~8.4 Sv (see Fig. 8). This is due in an equal part to enhanced diffusive upwelling as the NADW cell deepens into a region of higher diffusivity, and an increase in the clockwise eddy-induced cell in the convective region of the North Atlantic (as obtained from the Eulerian-mean and eddy-induced components of the MOC which are not shown).

Despite the lack of AABW formation, the anticlockwise PDW cell in the Pacific basin maintains its strength and expands over the full depth of the Pacific basin below the wind-driven gyres. Since isopycnals do not

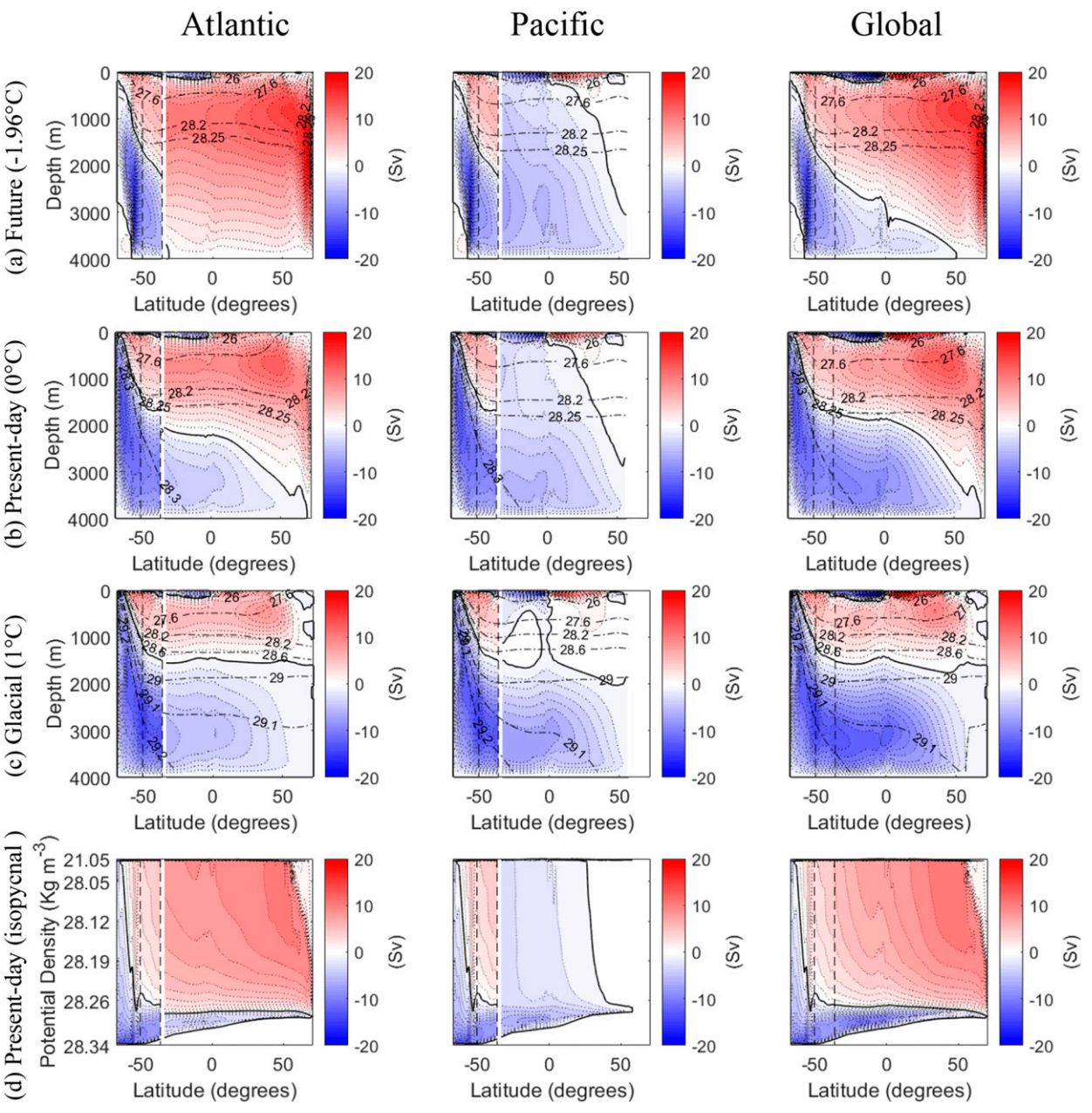

FIG. 4. Zonal-average net overturning streamfunction (1-Sv contour intervals) for varying sea ice freezing points (and MOC states) of (a) −1.96°C (future warmer state), (b) 0°C (present-day state), and (c) 1°C (glacial state) in depth space, and (d) 0°C (present-day state) in isopycnal space with a nonlinear density scale to highlight the deep ocean MOC. Shown are the (left) Atlantic, (center) Pacific, and (right) global-integrated circulations. The global-integrated streamfunction is plotted in the channel in all plots. Colors and contours are as in Figs. 2 and 3. Potential density contours are represented by thin dash–dot black lines [note the contour intervals above a potential density of 28.6 kg m^{-3} are greater in (c) than in (a) and (b)]. The vertical dashed lines are from left to right, the southernmost latitudes of the South America and South Africa landstrips, respectively.

outcrop in the north of the fresher Pacific basin, in contrast to the Atlantic basin, there is no upper cell to contract the anticlockwise lower cell. The connection between the upper NADW cell in the Atlantic basin and the lower cell in the Pacific basin provides most of the source water for the PDW cell and this must return to the Atlantic basin to conserve volume in each basin. We therefore suggest the structure of the PDW cell in the Pacific basin is largely controlled by the NADW pathways, specifically the magnitude of NADW_pac. The upwelled PDW which flows into the channel is almost entirely connected to the channel's upper cell (i.e., above

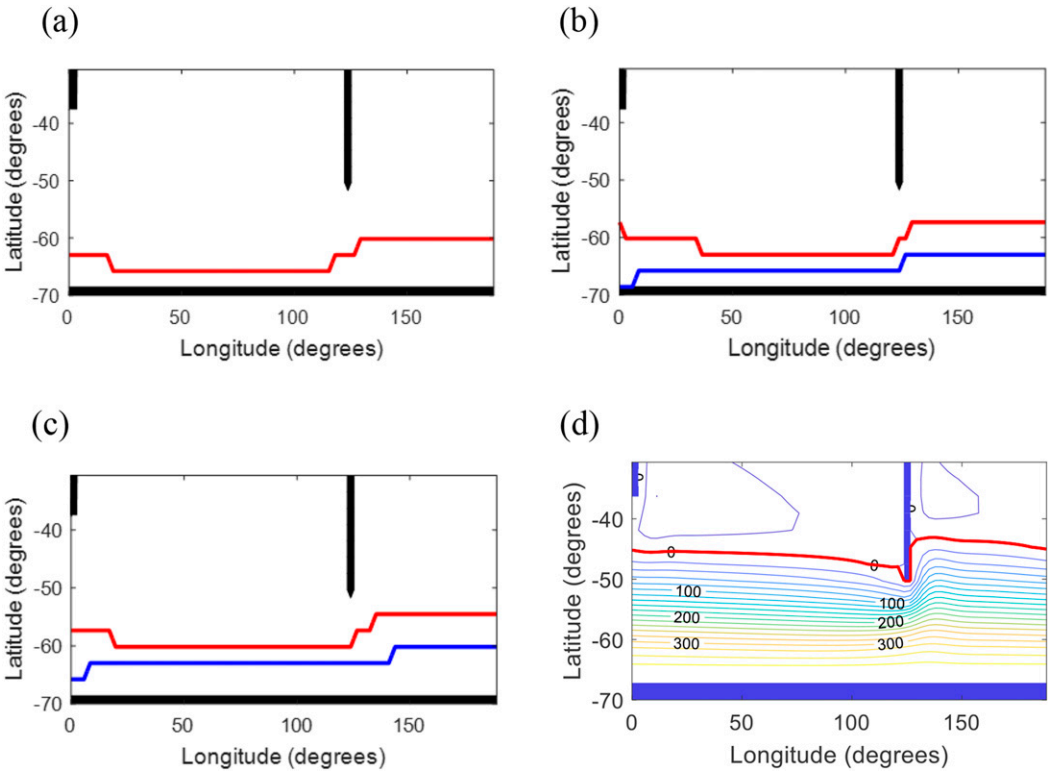

FIG. 5. Southern Ocean annual-average sea ice concentration for experiments with sea ice freezing points of (a) −1.96°C (future warmer state), (b) 0°C (present-day state), and (c) 1°C (glacial state). The sea ice concentration northern boundaries displayed are 0.1 (red) and 0.8 (blue) implying an ocean surface coverage by sea ice of 10% and 80%, respectively. (d) Barotropic streamfunction for the present-day control experiment [with contour intervals of 20 Sv and the 0-Sv streamline colored red (i.e., the most northerly streamline which circumvents the channel)].

the z_interface) at the channel–basin boundary. Thus, it is connected to the NADW cell in the Atlantic basin, rather than being an isolated cell (PDW_sep is zero). The PDW returns to the Atlantic basin either directly via the zonal flows or after further upwelling by the wind-driven upper cell in the channel (the latter pathway increases in this case).

b. *Present-day circulation*

The sea ice formation rate increases nonlinearly with an increased sea ice freezing point, reducing the annual-average buoyancy fluxes in the far south of the domain to negative values (see Fig. 6b). This increases the density in the south of the model and increases the formation of AABW and deep stratification. The lower AABW cell expands in the Atlantic basin while the NADW cell shoals. The NADW cell weakens as it is shoaled, with the greatest sensitivity to the sea ice formation rate (and buoyancy flux) between freezing points of −1° and 0.5°C (Fig. 8).

The MOC in the control experiment (described in section 3a) with a freezing point of 0°C (Fig. 4b) is most representative of the present-day MOC in this study, based on the Atlantic MOC structure. The NADW cell weakens by ~6.6 Sv relative to the future −1.96°C freezing point experiment, to ~13 Sv, somewhat weaker than the real ocean, while the Atlantic AABW cell probably upwells to slightly shallower depths than reality. However, given the similar structure of the control MOC in the Atlantic to reality, the pathways taken by the MOC in the present-day ocean are likely to be similar to this case, with the pathways depicted in Fig. 10b.

The depths of the NADW cell interface and the z_interface in this experiment decrease to ~2000 m and ~1700 m, respectively (see Fig. 9), and thus the ~300-m overlap between the Atlantic NADW cell and the channel's lower cell is far smaller than in the "warm" climate MOC. Therefore, the main change in the pathways taken in this present-day case relative to the warm climate MOC is that a greater proportion of the NADW flows into the upper wind-driven cell rather than the lower cell at the channel–basin boundary due to the shoaling of the NADW cell (see Fig. 4b). This leads to an

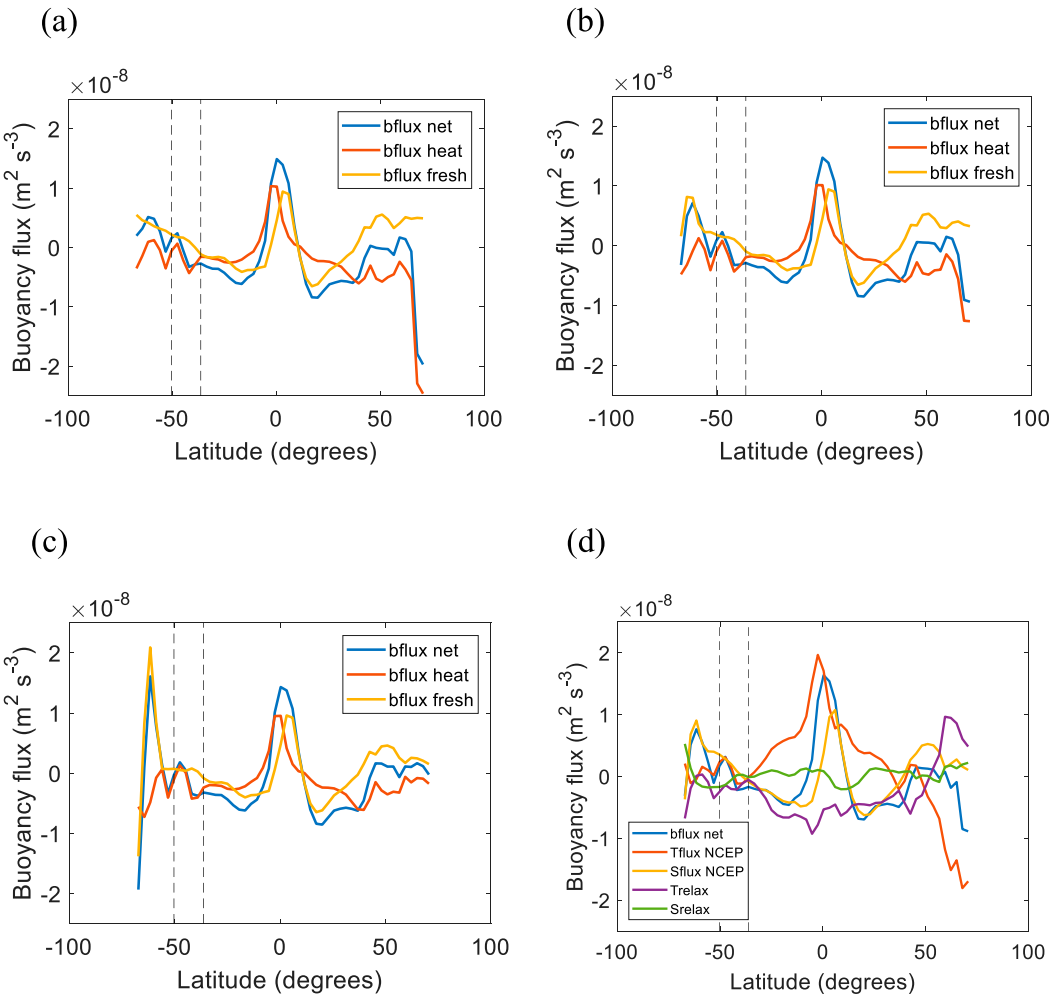

FIG. 6. Zonal-average surface buoyancy flux ($m^2 s^{-3}$) against latitude over the whole model domain; plotted is the net buoyancy flux (blue) and the heat (red) and freshwater (orange) flux contributions to the net buoyancy flux. The plots correspond to the experiments with a sea ice freezing point of (a) −1.96°C (future warmer state), (b) 0°C (present-day state), and (c) 1°C (glacial state). (d) The present-day state control buoyancy flux components, where "Tflux NCEP" and "Sflux NCEP" components are the heat and freshwater flux contributions calculated from NCEP data, and "Trelax" and "Srelax" components are the temperature and salinity relaxation flux contributions. These terms do not apply in regions of sea ice where there are no relaxation fluxes, although the net buoyancy flux is the true value, including sea ice effects.

increase in the volume of NADW flowing into the channel that is directly wind-driven (NADW_wind), which partially compensates for the decrease in the volume of NADW flowing along the Pacific pathway (NADW_pac) (see Fig. 8). The relative importance of these pathways in the present-day MOC is particularly sensitive to changes in Southern Ocean buoyancy forcing. There is now a direct zonal flow of NADW from the Atlantic to the Pacific basin above the z_interface (NADW_pac_upper) that also compensates for the large decrease in NADW_pac_lower. The deep pathway of NADW into the Pacific, NADW_pac_lower, now involves NADW upwelling adiabatically to the surface in the channel's lower cell before being transformed to denser AABW. The volume of NADW flowing into the channel (NADW_channel) only decreases by ~1.7 Sv, with most of the NADW cell weakening due to reduced Atlantic upwelling.

The PDW cell responds to these changes in NADW pathways to conserve volume in each basin. There is an increase in the PDW flowing into the channel's lower cell (PDW_sep), which is therefore isolated from the Atlantic basin. The volume of PDW which is upwelled further by the channel's upper wind-driven cell must decrease significantly regardless of changes in PDW cell strength and structure, since the NADW_wind component

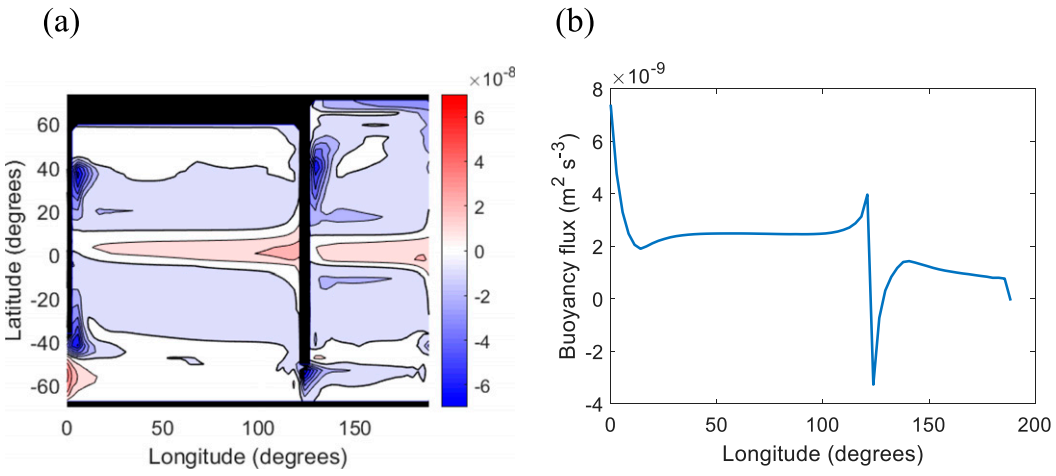

FIG. 7. (a) Surface distribution of surface buoyancy fluxes ($m^2 s^{-3}$) (with contour intervals of $1 \times 10^{-8} m^2 s^{-3}$ and the zero contour highlighted in black) and (b) the surface buoyancy flux against longitude in the southernmost latitude of the model domain. Both (a) and (b) correspond to the −1.96°C sea ice freezing point (future warmer state) experiment.

increases and there is also a slight decrease in the global-integrated flow into the channel's upper cell at the channel–basin boundary. Thus, a greater proportion of the PDW returning to the Atlantic must be via the direct zonal pathway. The PDW cell still upwells over the full depth of the Pacific basin (Fig. 4b).

c. Glacial circulation

As the sea ice freezing rate is increased further, the NADW cell continues to shoal and the AABW cell in the Atlantic basin expands. The NADW cell is more or less completely isolated from the channel's lower cell and the Pacific basin (see Fig. 4c). The magnitude of the negative buoyancy (and freshwater) flux in the south of the domain has increased significantly, while just to the north of this sea ice formation region, the positive buoyancy (and freshwater) flux has also increased due to the melting of sea ice formed farther south (see Fig. 6c).

The NADW cell weakens by ~4.4 Sv in the 1°C freezing point experiment relative to the control, to ~8.5 Sv (see Fig. 8). The mechanism responsible for the weakening and the change in pathways may well reflect the real world glacial circulation changes. The pathways taken in the glacial state are depicted in Fig. 9c. The overlap between the Atlantic NADW cell interface and the channel's lower cell is now only ~50 m (see Fig. 9). The flow of NADW into the channel (NADW_channel) decreases by ~3.1 Sv, explaining over two-thirds of the decrease in NADW cell strength. Of this reduced flow, the lower Pacific pathway (NADW_pac_lower) decreases by ~2.5 Sv to approximately zero due to the shoaling of the NADW cell. Thus, the AABW and NADW cells are virtually isolated (see Fig. 10c) with almost all of the upwelled PDW in the Pacific basin now flowing into the channel's lower cell (PDW_sep increases).

The direct wind pathway (NADW_wind) reduces by ~1.1 Sv in depth coordinates (Fig. 8b), although it is only reduced by ~0.1 Sv in isopycnal coordinates (Fig. 8c). The component is reduced as the z_interface is shoaled (all be it less so than the Atlantic NADW cell shoaling at the channel–basin boundary), while the reduction in PDW being upwelled further by the channel's upper cell opposes this decrease in NADW_wind. The NADW flowing into the channel is now almost all upwelled along the direct wind pathway (i.e., NADW_wind is approximately equal to NADW_channel). There is also a weak ~1.4-Sv direct zonal flow of NADW into an isolated PDW cell in the upper ocean (NADW_pac_upper), which maintains a small NADW_pac component (see Fig. 8), although this component is reduced to ~0.4 Sv in isopycnal coordinates (Fig. 8c). The volume of NADW upwelling in the Atlantic basin also decreases by ~1.3 Sv. Thus, changes in Atlantic basin upwelling play only a secondary role in the weakening between the present-day and glacial states. The shoaling of the NADW cell by enhanced sea ice formation provides a mechanism to both isolate the upper and lower cells and to weaken the NADW cell during glacial times.

d. Uncertainties in MOC component calculations

The meandering of the streamlines (i.e., standing eddies) in the channel can lead to errors when using depth-averaged coordinates since it does not account for zonal density variations. We only fully account for these effects by replotting in density space as described later

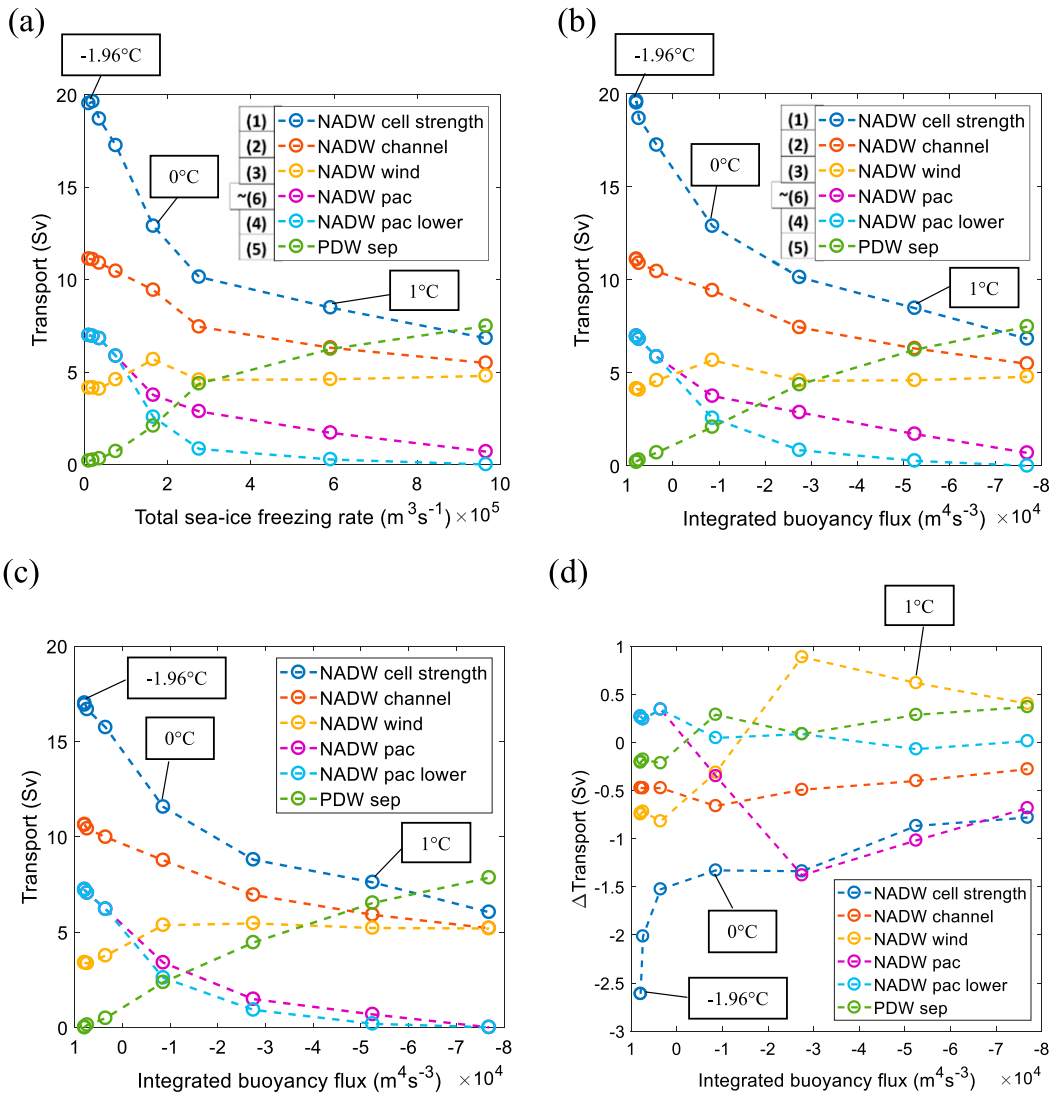

FIG. 8. Zonal-average net MOC overturning transport components as a function of (a) the total sea ice freezing rate in the Southern Ocean and (b) the area integrated buoyancy flux in the southernmost latitudes where the zonal-average buoyancy flux becomes negative as the sea ice formation rate increases. (c) Components as in (b), but using isopycnal coordinates. (d) Difference between isopycnal and depth coordinate components [i.e., (c) − (b)]. The dots on each component represent experiments with varying freezing points (see section 2) increasing from −1.96° to 1.5°C (corresponding to the lowest and highest freezing rates, respectively) with 0.5°C perturbations above −1.5°C. The colors and bracketed numbers next to the components plotted correspond to the components labeled in Fig. 3. The components plotted are as follows: (i) NADW cell strength (dark blue, 1), (ii) NADW_channel (red, 2), (iii) NADW_wind (yellow, 3), (iv) NADW_pac (purple, ~6), (v) NADW_pac_lower (light blue, 4), and vi) PDW_sep (green, 5). The NADW_wind, NADW_pac, and NADW_pac_lower components have been adjusted to account for any zonal flow of NADW into the Pacific basin above z_interface, or via the PDW upper-ocean streamfunction maxima below z_interface [see section 3b(2)]. The difference between the NADW cell strength (dark blue) and NADW_channel (red) is the volume of NADW that upwells in the Atlantic basin before reaching the channel. The difference between NADW_pac (purple) and NADW_pac_lower (light blue) is equal to NADW_pac_upper.

in this section. We also calculate the meridional overturning streamfunction along the 0-Sv barotropic streamline (the most northern streamline that circulates around the channel with a latitudinal deviation of ~8.5°). The depth of the cell interface is then shoaled by ~300 m in the warm state but only ~40 m in the present-day state, due to variations in the slope of the cell interface. However, this does not lead to an error in

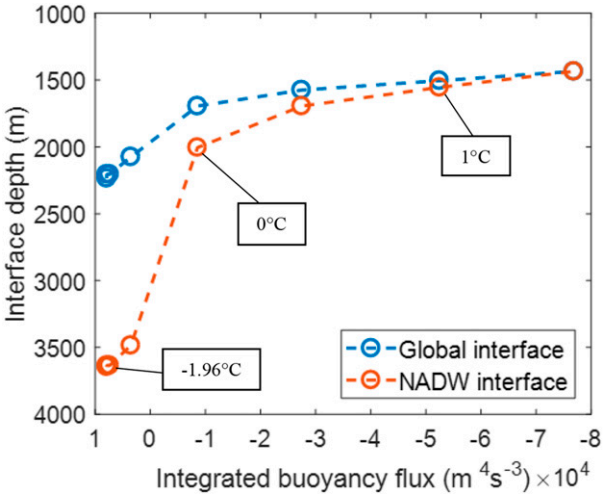

FIG. 9. Interface depth of the global-integrated circulation (blue) referred to as z_interface in this paper and the NADW cell (red) at the channel–basin boundary against the area integrated buoyancy flux in the southernmost latitudes where the zonal-average buoyancy flux becomes negative as the sea ice formation rate increases. Each dot corresponds to a varying freezing rate experiment (see Fig. 7).

the components calculated due to the fact the NADW is rapidly transported zonally across the channel north of this latitude (43.3°S), at 42°S, as can be seen in Fig. 5d, and is also seen in a tracer release experiment (not shown). Thus, the global-integrated streamfunction is appropriate at all latitudes south of about 42°S, a latitude with no meandering of the barotropic streamlines.

However, this still leaves an error due to calculating the components at the channel–basin boundary (36°S) rather than at 42°S, where the global-integrated flow is a good approximation. The error in the cell interface depth due to using the value at the channel–basin boundary rather than at 42°S (about 5.5° to the south) in our calculations leads to only a small error in the present-day and glacial states (only ~10 m in the present-day state) due to the shallow slope of the cell interface. It only becomes significant in the warm state where the cell interface has a steeper slope in the north of the channel, leading to an error of ~240 m in the cell interface depth. We use the meridional and vertical net velocities along the cell interface at the longitude of the Atlantic western boundary flow to calculate the change in depth of NADW as it flows south. Comparing this with the global-average change in depth suggests the NADW flowing south along the western boundary only upwells ~100 m less than the global-average flow between 36° and 42°S. This equates to an error of ~0.45 Sv, or an increase and decrease in NADW_pac and NADW_wind, respectively, equal to this magnitude, although PDW_sep is zero in this case and thus NADW_pac is unable to increase.

The streamfunction from which the component calculations described previously are made is in depth rather than density space. We also calculate the components in density space (see Fig. 8c) which provides confidence in our results since this is more accurate when considering ocean pathways. We use depth coordinates throughout this study since this is physically more intuitive and a comparison between these coordinate approaches is also interesting. The difference in the components calculated between these coordinate systems is small but significant. The main change when calculating in isopycnal space is a reduced NADW cell strength in the warm state due primarily to reduced Atlantic basin upwelling (see Figs. 8c,d). The other major difference is the increase in the upper Pacific pathway of NADW, NADW_pac_upper, between the warm and glacial states (specifically in the present-day state) is far smaller in isopycnal space. At freezing points above 0°C, this water instead flows along the direct wind pathway, NADW_wind, increasing this component and reducing the Pacific pathway, NADW_pac. The greatest change in these components occurs at a freezing point of 0.5°C in which NADW_pac and NADW_wind increase and decrease by ~0.9 Sv and ~1.4 Sv, respectively, relative to the calculations in depth space (see Fig. 8d). The upper Pacific pathway only increases to ~0.6 Sv rather than ~2 Sv. The overall change in the components is similar regardless of the coordinate system between the warm and glacial states (see Fig. 8d), although the compensation by an increasing upper Pacific pathway as the buoyancy forcing is varied from the present-day to a glacial state is smaller. The sensitivity of the direct wind and Pacific pathways to buoyancy forcing therefore increases when using isopycnal coordinates and thus while the quantitative results are affected by our choice to focus on the depth-averaged overturning, the qualitative results are shown to be robust.

5. Summary and conclusions

In this paper we have explored the dependence of the MOC strength and structure on variations in Southern Ocean buoyancy forcing, which is known from general theoretical considerations to play a major role in determining the relative size of the two main overturning cells in the ocean (Nikurashin and Vallis 2012). Specifically, we have used a two-basin ocean model with idealized topography to analyze the sensitivity of the MOC to varying Southern Ocean sea ice formation, one of the main mechanisms proposed to cause the transition of the ocean circulation to a glacial state (Ferrari et al. 2014; Jansen and Nadeau 2016; Nadeau et al. 2019).

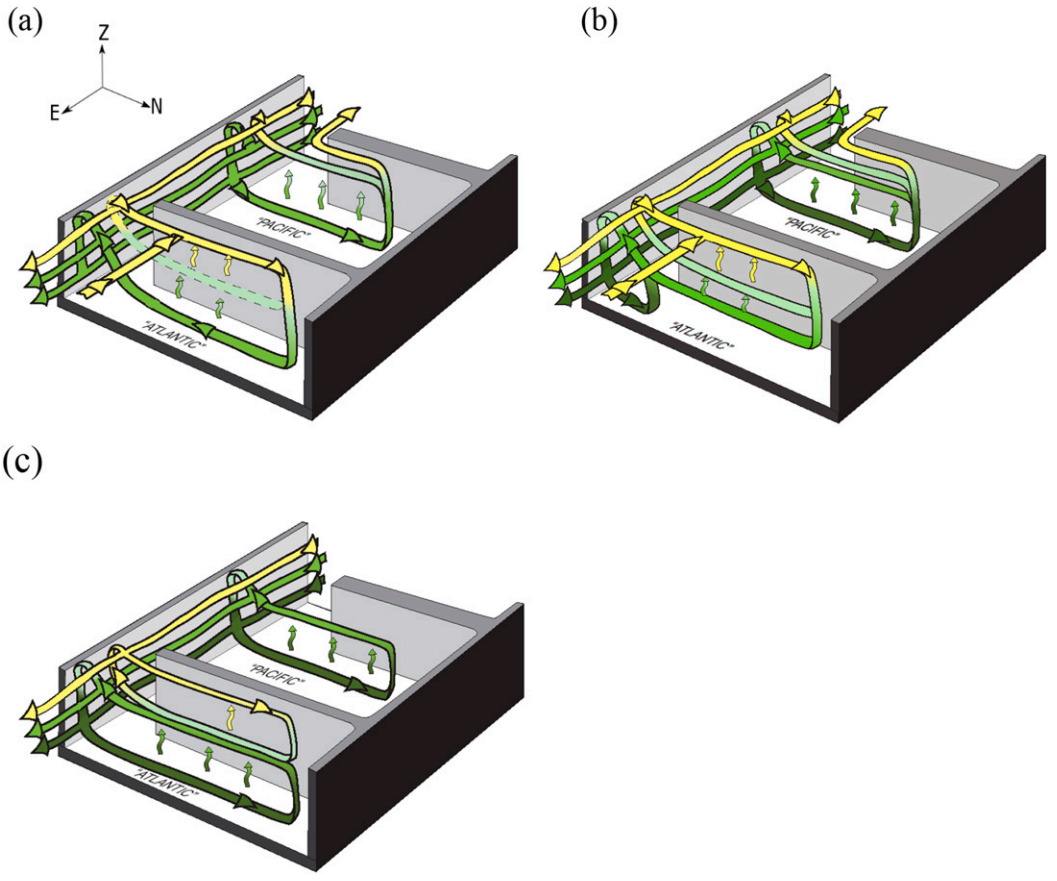

FIG. 10. Schematics of MOC pathways in (a) the future warmer, (b) present-day, and (c) glacial states of the two-basin model. Colors represent increasing density of flows from yellow (least dense) through lightest green to darkest green (most dense). Diffusive upwelling is indicated by small vertical wavy arrows. In (a) there is almost no Southern Ocean sea ice formation, which however increases progressively in (b) and then (c). The meridional pathways represent the zonal-average flow in each basin and over the channel. The figures illustrate the shoaling of the NADW cell in the Atlantic in response to progressively greater buoyancy forcing in the south. For detailed explanation, see the text. The dashed line pathway [in (a)] of less dense NADW in the Atlantic basin flowing into the upper wind-driven cell in the channel represents the fact that the flow along this pathway is weaker than along the deeper pathway of NADW into the channel's lower cell.

We find that enhanced sea ice formation in the Southern Ocean, and thus more negative Southern Ocean buoyancy fluxes, can explain the transition of the MOC from a present-day to a glacial state (in agreement with the aforementioned studies) with an expanded AABW cell and weakened, shallow, NADW cell. In this glacial state the upper and lower cells are effectively isolated from each other and, in particular, the NADW is largely driven by the channel's upper wind-driven cell, with little influence of diffusive upwelling in the Pacific. In contrast, in a potential future warm climate, with more positive Southern Ocean buoyancy fluxes, the ocean is characterized by a weaker or nonexistent AABW cell in the Atlantic and a deeper and stronger NADW cell [in agreement with the Jansen et al. (2018) warming-induced response of the steady state MOC in a single-basin model]. The NADW (in the Atlantic) and the abyssal water mass in the Pacific (analogous to AABW) then have similar densities, with the deep ocean being only very weakly stratified.

A shoaling of the depth of the isopycnal defining the northern boundary of summertime Southern Ocean sea ice due to the equatorward expansion of sea ice (Ferrari et al. 2014), and enhanced abyssal stratification as Southern Ocean sea ice formation increases (Jansen and Nadeau 2016) are likely to both play an important role in causing the NADW cell to shoal (Nadeau et al. 2019). The change in the MOC pathways described here is a consequence of the sea ice induced shoaling of the NADW cell (whatever the cause of the shoaling may be).

We have argued that the pathways taken by the MOC in these aforementioned regimes may be determined

from the volume flow rates between the net circulations in each basin and the global-integrated net circulation in the channel. The direct wind and Pacific pathways of the NADW cell can thus be separated. The direct wind pathway of the NADW cell is equal to the volume of NADW flowing into the channel above the interface between the channel's upper and lower cells at the channel–basin boundary (i.e., into the channel's upper cell). Conversely, the volume of NADW that ultimately upwells diffusively in the Pacific basin (the Pacific pathway of NADW), either after upwelling and consequently sinking in the Southern Ocean, or by flowing directly into the Pacific basin via zonal flows as discussed by Ferrari et al. (2017), is equal to the volume of NADW flowing into the channel below the cell interface (i.e., into the channel's lower cell). These components are modified slightly by accounting for any NADW which flows zonally into the Pacific basin above the cell interface.

The role played by both wind and diffusive upwelling in contributing to the present-day AMOC strength then becomes apparent and will be further quantified in Part II. In our present-day climate simulations, the direct wind pathway via upwelling in the Southern Ocean has about the same magnitude as the Pacific pathway via diffusive upwelling in the Pacific, with Atlantic basin upwelling playing a secondary role, although this result of course depends on the precise values of the parameters chosen.

As the Southern Ocean sea ice formation rate is increased (leading to enhanced negative buoyancy fluxes in regions of sea ice growth because of seasonal brine rejection), the proportion of NADW flowing along the direct wind pathway relative to that which flows along the Pacific pathway increases. For small changes in sea ice formation the direct wind pathway increase partially compensates for the decrease in the Pacific pathway. As the sea ice formation rate continues to increase, the connection between the upper and lower cells, and thus between the Atlantic and Pacific basins is reduced further. Eventually the cells are completely isolated with the Pacific pathway associated with diffusive upwelling by the dominant deep PDW cell in the Pacific no longer contributing to the NADW cell strength. This is our glacial state.

The changes in these pathways are caused by the shoaling of the NADW cell at the channel–basin boundary as the Southern Ocean sea ice formation rate is increased causing the NADW flowing into the channel to be confined to shallower regions. Now, NADW can in principle either flow directly into the channel's wind-driven upper cell, or into the lower cell which ultimately upwells diffusively in the Pacific basin. But as the NADW cell is shoaled, the volume of NADW flowing into the channel's lower cell decreases and the cell therefore becomes increasingly directed along the direct wind pathway as the Southern Ocean buoyancy flux becomes more negative. The relative size of the aforementioned pathways under a given Southern Ocean buoyancy forcing depends on the strength of the Southern Ocean winds and the vertical diffusivity profile within the basins, as will be further explored in Part II of this study.

In the present-day MOC both the direct wind and the Pacific pathways of NADW are important, and the relative size of these pathways is very sensitive to perturbations in the Southern Ocean buoyancy forcing. There is also a weak direct zonal flow of NADW into the upper Pacific. A proportion of the upwelled PDW flows into the Atlantic basin via zonal flows and the channel's upper wind-driven cell, in order to conserve volume in each basin. The remainder flows into the channel's lower cell which is isolated from the Atlantic basin's NADW cell. The upwelling of PDW to shallow depths is possible despite a far lower diffusivity in the upper ocean.

The potential future warm climate MOC, in which Southern Ocean sea ice formation almost ceases, leads to a deepening and slight strengthening of the NADW cell relative to the present-day, predominately due to enhanced Atlantic basin upwelling. The NADW cell primarily flows along the Pacific pathway under these forcings with most NADW flowing directly into the channel's lower cell and thence into the Pacific basin. The PDW cell responds by returning all of the diffusively upwelled PDW to the Atlantic basin via the same pathways as in the present-day MOC. This is despite there being virtually no AABW formation in a largely unstratified deep ocean.

In the glacial state MOC, the NADW cell weakens and is shoaled significantly while the AABW cell expands. Thus, NADW can only flow into the channel's upper wind-driven cell (and the upper Pacific). There is no longer any flow into the channel's lower cell and hence the lower Pacific pathway of NADW reduces to zero with almost all NADW flowing into the channel flowing along the direct wind pathway. The NADW cell is therefore primarily weakened by a reduced flow into the channel. The AABW cell in the Pacific basin responds by shoaling to the deep ocean rather than upwelling to the surface, with all of the upwelled PDW in the deep ocean flowing into the channel's lower cell. This again conserves volume in each basin. The NADW and AABW cells are therefore completely isolated.

This study extends our understanding of the pathways taken by the MOC under varying buoyancy forcings, following on from the study of Ferrari et al. (2014) and

Nadeau et al. (2019). It improves our understanding of the transition of the MOC between varying buoyancy states through eight varying Southern Ocean sea ice formation simulations including a warmer than present-day state. Most previous studies only show a present-day and glacial state MOC. In particular, the pathways taken by PDW in addition to NADW are made explicit (Nadeau et al. (2019) focused on the NADW pathways), including the response of the PDW cell to changes in the NADW pathways. The variation of the pathways taken by both NADW and PDW flowing into the channel through changes in the volume flow rates into the channel's upper and lower cells, and changes in direct zonal exchanges helps us to explain the buoyancy-induced changes in the strength and structure of the MOC. The meridional overturning streamfunction is shown to be a very useful tool to quantitatively evaluate the MOC pathways.

The transition to an ocean circulation resembling the one at the last glacial maximum, with a larger bottom cell (at least in the Atlantic) and weaker NADW cell, is undoubtedly influenced by many factors, including ice sheet formation in the Northern Hemisphere (Eisenman et al. 2009; Vettoretti and Peltier 2013) and possibly an overall reduction in temperature changing the relative importance of temperature and salinity terms in the equation of state (e.g., De Boer et al. 2008). Here we show support for the interpretation that changes in Southern Ocean sea ice almost certainly play a major role in that transition.

Acknowledgments. We greatly appreciate and thank Jonathan Lauderdale for his advice on using the MITgcm, and Tobia Tudino for his help in using the university supercomputer. JAB and AJW thank the Royal Society for funding via a Research Professorship held by AJW. GKV acknowledges support from the "Leverhulme Trust."

APPENDIX

Methods: Calculation of the Overturning Components

The streamfunction components described below are analyzed at the latitude bounding the north of the channel (36°S). The term ψ_{chan} is the global-integrated streamfunction at 36°S while ψ_{NADW} and ψ_{PDW} are the absolute values of the NADW and PDW streamfunctions at the south of the Atlantic and Pacific basins, respectively (i.e., at 36°S). The subscript "max" is the maximum value at 36°S. The ocean depth z increases below the surface ($z = 0$). The following formulas are used to determine the MOC components labeled in Fig. 3 and used throughout this study. It should, however, be noted that the upper maxima of PDW (present in some cases) is only accounted for in these equations if the upper maxima is isolated above z_interface, otherwise a slight modification to (A3), (A4), (A6), and (A7) is required:

$$\text{z\_interface} = z\big|_{\psi_{\text{chan}}} = 0, \tag{A1}$$

$$\begin{aligned}\text{NADW\_channel} &= T_{\text{NADW\_channel}}\\ &= \psi_{\text{NADW\_max}}\big|_{y=36°\text{S}},\end{aligned} \tag{A2}$$

$$\begin{aligned}\text{NADW\_pac\_lower} &= T_{\text{NADW\_pac\_lower}}\\ &= \psi_{\text{NADW}}\big|_{z=\text{interface}},\end{aligned} \tag{A3}$$

$$\begin{aligned}\text{NADW\_pac\_upper} &= T_{\text{NADW\_pac\_upper}}\\ &= \psi_{\text{PDW\_max}}\big|_{z\le \text{z\_interface}} - T_{\text{NADW\_pac\_lower}},\end{aligned} \tag{A4}$$

$$\begin{aligned}\text{NADW\_pac} &= T_{\text{NADW\_pac}} = T_{\text{NADW\_pac\_lower}}\\ &\quad + T_{\text{NADW\_pac\_upper}},\end{aligned} \tag{A5}$$

$$\begin{aligned}\text{NADW\_wind} &= T_{\text{NADW\_wind}}\\ &= T_{\text{NADW\_channel}} - T_{\text{NADW\_pac}},\end{aligned} \tag{A6}$$

$$\begin{aligned}\text{PDW\_sep} &= T_{\text{PDW\_sep}} = \psi_{\text{PDW\_max}}\big|_{y=36°\text{S}}\\ &\quad - \psi_{\text{PDW}}\big|_{z=\text{interface}}, \quad \text{and}\end{aligned} \tag{A7}$$

$$\begin{aligned}\text{PDW\_at} &= T_{\text{PDW\_at}} = \psi_{\text{PDW\_max}}\big|_{y=36°\text{S}}\\ &\quad - T_{\text{PDW\_sep}} + T_{\text{NADW\_pac\_upper}}.\end{aligned} \tag{A8}$$

Theoretically,

$$T_{\text{NADW\_pac}} = T_{\text{PDW\_at}}, \tag{A9}$$

in order to satisfy the conservation of volume, since the flow of PDW which returns to the Atlantic basin to form NADW, $T_{\text{PDW\_at}}$, should be equal to the volume of NADW that ultimately flows into the Pacific basin, $T_{\text{NADW\_pac}}$.

Substituting (A5) and (A8) into (A9), and rearranging gives

$$\psi_{\text{PDW\_max}}\big|_{y=36°\text{S}} = T_{\text{NADW\_pac\_lower}} + T_{\text{PDW\_sep}}. \tag{A10}$$

The sum of $T_{\text{NADW\_pac\_lower}}$ and $T_{\text{PDW\_sep}}$ is compared to the magnitude of the PDW cell maxima at the channel–basin boundary, $\psi_{\text{PDW\_max}}\big|_{y=36°\text{S}}$ to test the method. These should be equal if (A8) is satisfied.

The sum of the components on the rhs of (A10) are consistently greater than the maxima of the PDW cell, although only by at most ~0.4 and ~0.1 Sv in the depth

and isopycnal-averaged coordinate calculations, respectively. This is a small difference when compared to the magnitude of the transports involved in (A10) and is always in the same direction despite large changes in the transports between experiments. This small difference is due to the streamfunction of the individual basins in fact only being obtained at 37.4°S, half a grid space to the north of the channel–basin boundary (36°S) due to the channel–basin boundary being located between the meridional velocity grid points and thus requiring interpolation. The streamfunction of the individual basin sectors cannot be defined south of the channel–basin boundary and thus only the global-average streamfunction is obtained at the boundary itself. Since the discrepancy is small and always in the same direction, it does not alter the conclusions drawn in this paper.

REFERENCES

Abernathey, R., I. Cerovečki, P. R. Holland, E. Newsom, M. Mazloff, and L. D. Talley, 2016: Water-mass transformation by sea ice in the upper branch of the Southern Ocean overturning.. *Nat. Geosci.*, **9**, 596–601, https://doi.org/10.1038/ngeo2749.

Adkins, J. F., K. McIntyre, and D. P. Schrag, 2002: The salinity, temperature, and $\delta_{18}O$ of the glacial deep ocean. *Science*, **298**, 1769–1773, https://doi.org/10.1126/science.1076252.

Broecker, W. S., 1987: The biggest chill. *Natural History*, Vol. 96 (Oct.), 74–82.

——, and T.-H. Peng, 1982: *Tracers in the Sea*. Eldigio Press, 690 pp.

Bryan, K., and L. J. Lewis, 1979: A water mass model of the world ocean. *J. Geophys. Res.*, **84**, 2503–2517, https://doi.org/10.1029/JC084iC05p02503.

Burke, A., A. L. Stewart, J. F. Adkins, R. Ferrari, M. F. Jansen, and A. F. Thompson, 2015: The glacial mid-depth radiocarbon bulge and its implications for the overturning circulation. *Paleoceanography*, **30**, 1021–1039, https://doi.org/10.1002/2015PA002778.

Cessi, P., 2019: The global overturning circulation. *Annu. Rev. Mar. Sci.*, **11**, 249–270, https://doi.org/10.1146/annurev-marine-010318-095241.

Curry, W., and D. Oppo, 2005: Glacial water mass geometry and the distribution of $\delta^{13}C$ of $\sum CO_2$ in the western Atlantic Ocean. *Paleoceanography*, **20**, PA1017, https://doi.org/10.1029/2004PA001021.

De Boer, A. M., J. R. Toggweiler, and D. M. Sigman, 2008: Atlantic dominance of the meridional overturning circulation. *J. Phys. Oceanogr.*, **38**, 435–450, https://doi.org/10.1175/2007JPO3731.1.

Doos, K., and A. Coward, 1997: The Southern Ocean as the major upwelling zone of North Atlantic deep water. *International WOCE Newsletter*, No. 27, WOCE International Project Office, Southampton, United Kingdom, 3–4.

Duplessy, J., N. Shackleton, R. Fairbanks, L. Labeyrie, D. Oppo, and N. Kallel, 1988: Deepwater source variations during the last climatic cycle and their impact on the global deepwater circulation. *Paleoceanography*, **3**, 343–360, https://doi.org/10.1029/PA003i003p00343.

Eady, E. T., 1957: The general circulation of the atmosphere and oceans. *The Earth and Its Atmosphere*, D. R. Bates, Ed., Basic Books, 131–151.

Eisenman, I., C. M. Bitz, and E. Tziperman, 2009: Rain driven by receding ice sheets as a cause of past climate change. *Paleoceanography*, **24**, PA4209, https://doi.org/10.1029/2009PA001778.

Ferrari, R., M. F. Jansen, J. F. Adkins, A. Burke, A. L. Stewart, and A. F. Thompson, 2014: Antarctic sea ice control on ocean circulation in present and glacial climates. *Proc. Natl. Acad. Sci. USA*, **111**, 8753–8758, https://doi.org/10.1073/pnas.1323922111.

——, L. P. Nadeau, D. P. Marshall, L. C. Allison, and H. L. Johnson, 2017: A model of the ocean overturning circulation with two closed basins and a reentrant channel. *J. Phys. Oceanogr.*, **47**, 2887–2906, https://doi.org/10.1175/JPO-D-16-0223.1.

Gent, P. R., and J. C. McWilliams, 1990: Isopycnal mixing in ocean circulation models. *J. Phys. Oceanogr.*, **20**, 150–155, https://doi.org/10.1175/1520-0485(1990)020<0150:IMIOCM>2.0.CO;2.

——, J. Willebrand, T. J. McDougall, and J. C. McWilliams, 1995: Parameterizing eddy-induced tracer transports in ocean circulation models. *J. Phys. Oceanogr.*, **25**, 463–474, https://doi.org/10.1175/1520-0485(1995)025<0463:PEITTI>2.0.CO;2.

Gnanadesikan, A., 1999: A simple predictive model for the structure of the oceanic pycnocline. *Science*, **283**, 2077–2079, https://doi.org/10.1126/science.283.5410.2077.

Gordon, A. L., 1986: Interocean exchange of thermocline water. *J. Geophys. Res.*, **91**, 5037–5046, https://doi.org/10.1029/JC091iC04p05037.

Griffies, S. M., and Coauthors, 2009: Coordinated ocean-ice reference experiments (COREs). *Ocean Modell.*, **26**, 1–46, https://doi.org/10.1016/j.ocemod.2008.08.007.

Hibler, W. D., III, 1979: A dynamic thermodynamic sea ice model. *J. Phys. Oceanogr.*, **9**, 815–846, https://doi.org/10.1175/1520-0485(1979)009<0815:ADTSIM>2.0.CO;2.

——, 1980: Modeling a variable thickness sea ice cover. *Mon. Wea. Rev.*, **108**, 1943–1973, https://doi.org/10.1175/1520-0493(1980)108<1943:MAVTSI>2.0.CO;2.

Ito, T., and J. Marshall, 2008: Control of lower-limb overturning circulation in the Southern Ocean by diapycnal mixing and mesoscale eddy transfer. *J. Phys. Oceanogr.*, **38**, 2832–2845, https://doi.org/10.1175/2008JPO3878.1.

Jansen, M. F., 2017: Glacial ocean circulation and stratification explained by reduced atmospheric temperature. *Proc. Natl. Acad. Sci. USA*, **114**, 45–50, https://doi.org/10.1073/pnas.1610438113.

——, and L. P. Nadeau, 2016: The effect of Southern Ocean surface buoyancy loss on the deep-ocean circulation and stratification. *J. Phys. Oceanogr.*, **46**, 3455–3470, https://doi.org/10.1175/JPO-D-16-0084.1.

——, ——, and T. M. Merlis, 2018: Transient versus equilibrium response of the ocean's overturning circulation to warming. *J. Climate*, **31**, 5147–5163, https://doi.org/10.1175/JCLI-D-17-0797.1.

Kalnay, E., and Coauthors, 1996: The NCEP/NCAR 40-Year Reanalysis Project. *Bull. Amer. Meteor. Soc.*, **77**, 437–472, https://doi.org/10.1175/1520-0477(1996)077<0437:TNYRP>2.0.CO;2.

Klockmann, M., U. Mikolajewicz, and J. Marotzke, 2018: Two AMOC states in response to decreasing greenhouse gas concentrations in the coupled climate model MPI-ESM. *J. Climate*, **31**, 7969–7984, https://doi.org/10.1175/JCLI-D-17-0859.1.

Lauderdale, J. M., A. C. Naveira Garabato, K. I. C. Oliver, M. J. Follows, and R. G. Williams, 2013: Wind-driven changes in Southern Ocean residual circulation, ocean carbon reservoirs and atmospheric CO_2. *Climate Dyn.*, **41**, 2145–2164, https://doi.org/10.1007/s00382-012-1650-3.

Levitus, S., and T. P. Boyer, 1994a: *Salinity*. Vol. 3, *World Ocean Atlas 1994*, NOAA Atlas NESDIS 3, 99 pp.

——, and ——, 1994b: *Temperature*. Vol. 4, *World Ocean Atlas 1994*, NOAA Atlas NESDIS 4, 117 pp.

Liu, Z., S. Shin, R. Webb, W. Lewis, and B. Otto-Bliesner, 2005: Atmospheric CO_2 forcing on glacial thermohaline circulation and climate. *Geophys. Res. Lett.*, **32**, L02706, https://doi.org/10.1029/2004GL021929.

Losch, M., D. Menemenlis, J.-M. Campin, P. Heimbach, and C. Hill, 2010: On the formulation of sea-ice models. Part 1: Effects of different solver implementations and parameterizations. *Ocean Modell.*, **33**, 129–144, https://doi.org/10.1016/j.ocemod.2009.12.008.

Lumpkin, R., and K. Speer, 2007: Global ocean meridional overturning. *J. Phys. Oceanogr.*, **37**, 2550–2562, https://doi.org/10.1175/JPO3130.1.

Lynch-Stieglitz, J., W. B. Curry, and N. Slowey, 1999: Weaker Gulf stream in the Florida straits during the last glacial maximum. *Nature*, **402**, 644–648, https://doi.org/10.1038/45204.

Marshall, J., and T. Radko, 2003: Residual mean solutions for the Antarctic Circumpolar Current and its associated overturning circulation. *J. Phys. Oceanogr.*, **33**, 2341–2354, https://doi.org/10.1175/1520-0485(2003)033<2341:RSFTAC>2.0.CO;2.

——, A. Adcroft, C. Hill, L. Perelman, and C. Heisey, 1997a: A finite-volume, incompressible Navier Stokes model for studies of the ocean on parallel computers. *J. Geophys. Res.*, **102**, 5753–5766, https://doi.org/10.1029/96JC02775.

——, C. Hill, L. Perelman, and A. Adcroft, 1997b: Hydrostatic, quasi-hydrostatic, and nonhydrostatic ocean modelling. *J. Geophys. Res.*, **102**, 5733–5752, https://doi.org/10.1029/96JC02776.

McManus, J., R. Francois, J. M. Gherardi, L. Keigwin, and S. Brown-Leger, 2004: Collapse and rapid resumption of Atlantic meridional circulation linked to deglacial climate changes. *Nature*, **428**, 834–837, https://doi.org/10.1038/nature02494.

Muglia, J., and A. Schmittner, 2015: Glacial Atlantic overturning increased by wind stress in climate models. *Geophys. Res. Lett.*, **42**, 9862–9868, https://doi.org/10.1002/2015GL064583.

Nadeau, L.-P., R. Ferrari, and M. F. Jansen, 2019: Antarctic sea ice control on the depth of North Atlantic deep water. *J. Climate*, **32**, 2537–2551, https://doi.org/10.1175/JCLI-D-18-0519.1.

Nikurashin, M., and G. Vallis, 2011: A theory of deep stratification and overturning circulation in the ocean. *J. Phys. Oceanogr.*, **41**, 485–502, https://doi.org/10.1175/2010JPO4529.1.

——, and ——, 2012: A theory of the interhemispheric meridional overturning circulation and associated stratification. *J. Phys. Oceanogr.*, **42**, 1652–1667, https://doi.org/10.1175/JPO-D-11-0189.1.

Redi, M. H., 1982: Oceanic isopycnal mixing by coordinate rotation. *J. Phys. Oceanogr.*, **12**, 1154–1158, https://doi.org/10.1175/1520-0485(1982)012<1154:OIMBCR>2.0.CO;2.

Richardson, P. L., 2008: On the history of meridional overturning circulation schematic diagrams. *Prog. Oceanogr.*, **76**, 466–486, https://doi.org/10.1016/j.pocean.2008.01.005.

Schmitz, W. J., Jr., 1995: On the interbasin-scale thermohaline circulation. *Rev. Geophys.*, **33**, 151–173, https://doi.org/10.1029/95RG00879.

Shakespeare, C. J., and A. M. Hogg, 2012: An analytical model of the response of the meridional overturning circulation to changes in wind and buoyancy forcing. *J. Phys. Oceanogr.*, **42**, 1270–1287, https://doi.org/10.1175/JPO-D-11-0198.1.

Shin, S.-I., Z. Liu, B. L. Otto-Bliesner, J. E. Kutzbach, and S. J. Vavrus, 2003: Southern Ocean sea-ice control of the glacial North Atlantic thermohaline circulation. *Geophys. Res. Lett.*, **30**, 1096, https://doi.org/10.1029/2002GL015513.

Sun, S., I. Eisenman, and A. L. Stewart, 2016: The influence of Southern Ocean surface buoyancy forcing on glacial-interglacial changes in the global deep ocean stratification. *Geophys. Res. Lett.*, **43**, 8124–8132, https://doi.org/10.1002/2016GL070058.

Talley, L. D., 2013: Closure of the global overturning circulation through the Indian, Pacific, and Southern Oceans: Schematics and transports. *Oceanography*, **26**, 80–97, https://doi.org/10.5670/oceanog.2013.07.

Thompson, A. F., A. Stewart, and T. Bischoff, 2016: A multibasin residual-mean model for the global overturning circulation. *J. Phys. Oceanogr.*, **46**, 2583–2604, https://doi.org/10.1175/JPO-D-15-0204.1.

Toggweiler, J. R., and B. Samuels, 1993: New radiocarbon constraints on the upwelling of abyssal water to the ocean's surface. *The Global Carbon Cycle*, M. Heimann, Ed., Vol. 15, Springer-Verlag, 334–366.

——, and ——, 1995: Effect of Drake Passage on the global thermohaline circulation. *Deep-Sea Res. I*, **42**, 477–500, https://doi.org/10.1016/0967-0637(95)00012-U.

——, J. L. Russell, and S. R. Carson, 2006: Midlatitude westerlies, atmospheric CO_2, and climate change during the ice ages. *Paleoceanography*, **21**, PA2005, https://doi.org/10.1029/2005PA001154.

Vallis, G. K., 2000: Large-scale circulation and production of stratification: Effects of wind, geometry, and diffusion. *J. Phys. Oceanogr.*, **30**, 933–954, https://doi.org/10.1175/1520-0485(2000)030<0933:LSCAPO>2.0.CO;2.

——, 2017: *Atmospheric and Oceanic Fluid Dynamics*. Cambridge University Press, 946 pp.

Vettoretti, G., and W. R. Peltier, 2013: Last Glacial Maximum ice sheet impacts on North Atlantic climate variability: The importance of the sea ice lid. *Geophys. Res. Lett.*, **40**, 6378–6383, https://doi.org/10.1002/2013GL058486.

Watson, A. J., and A. C. N. Garabato, 2006: The role of Southern Ocean mixing and upwelling in glacial–interglacial atmospheric CO_2 change. *Tellus*, **58B**, 73–87, https://doi.org/10.1111/j.1600-0889.2005.00167.x.

——, G. K. Vallis, and M. Nikurashin, 2015: Southern Ocean buoyancy forcing of ocean ventilation and glacial atmospheric CO_2. *Nat. Geosci.*, **8**, 861–864, https://doi.org/10.1038/ngeo2538.

Wolfe, C. L., and P. Cessi, 2009: Overturning circulation in an eddy-resolving model: The effect of the pole-to-pole temperature gradient. *J. Phys. Oceanogr.*, **39**, 125–142, https://doi.org/10.1175/2008JPO3991.1.

——, and ——, 2011: The adiabatic pole-to-pole overturning circulation. *J. Phys. Oceanogr.*, **41**, 1795–1810, https://doi.org/10.1175/2011JPO4570.1.

Wunsch, C., and R. Ferrari, 2004: Vertical mixing, energy, and the general circulation of the oceans. *Annu. Rev. Fluid Mech.*, **36**, 281–314, https://doi.org/10.1146/annurev.fluid.36.050802.122121.

Zhang, J., and W. D. Hibler III, 1997: On an efficient numerical method for modeling sea ice dynamics. *J. Geophys. Res.*, **102**, 8691–8702, https://doi.org/10.1029/96JC03744.